Chapter 4 – Equilibrium and Flux Surface Integrity

This chapter discusses the NCSX equilibrium calculations, including the issue of flux surface integrity. The VMEC equilibrium code has been used for the routine generation of three-dimensional equilibria for stability and transport studies, and it has been incorporated in the optimizer for generating candidate NCSX configurations and assessing coilset flexibility. The code is described in Section 4.1. Equilibrium calculations have been done with bootstrap-consistent current profiles, and the calculation of the bootstrap current is discussed in Section 4.2. Calculation of three-dimensional equilibria with islands and stochastic regions has been done with the PIES code, and the code is described in Section 4.3. Section 4.4 discusses the evaluation of flux surfaces for candidate configurations generated by the optimizer. Section 4.5 describes a method that has been used to make small modifications to the NCSX configuration to heal residual magnetic islands. A set of trim coils provides flexibility in the experiment to adjust resonant field components for a range of configurations. The calculations described in sections 4.3-4.5 do not include neoclassical effects, which reduce island widths, and the likely consequences of these effects are estimated in Section 4.6.

4.1 VMEC

The VMEC code[1] solves the three-dimensional equilibrium equations using a representation for the magnetic field that assumes nested flux surfaces. VMEC uses an inverse moments method, in which the geometric coordinates R and Z are expanded in Fourier series in both a poloidal angle variable and the toroidal angle(for three dimensions). The coefficients Rmn, Zmn in this series expansion are functions of the normalized toroidal flux s, where s = 0 is the magnetic axis (which can be a helical curve in three dimensions) and s = 1 is the plasma boundary. Here, m is the poloidal and n is the toroidal Fourier mode number. The boundary Fourier coefficients Rmn(1) and Zmn(1) can either be constant (corresponding to a "fixed-boundary" equilibrium calculation), or they may be self-consistently computed from the MHD force balance equation at the plasma-vacuum boundary (for a "free-boundary" calculation[2]). Internally, VMEC computes an addition "renormalization" stream function (λ) which is used to optimize, dynamically and at every radial surface, the convergence rate in Fourier space for the spectral sum Σ(Rmn**2 + Zmn**2). In the original VMEC, radial mesh gridding is staggered, with the Rmn(s) and Zmn(s) coefficients defined on integral radial mesh points sj = (j-1)/(Ns-1) [where Ns is the number of radial nodes] and the lambda coefficients on half-integer mesh points interleaving the Rmn, Zmn mesh. This scheme has been proven to lead to excellent radial resolution as well as minimal mesh separation (at least for large aspect ratio plasmas and with limited angular resolution meshes).

Significant improvements have been made to the VMEC code in the context of the NCSX design effort. It has been redifferenced to improve the convergence both on finer angular and radial meshes as well as for equilibria with a wide range of rotational transform profiles. In VMEC, the inverse equations are cast as second order equations (in radius) for the Fourier components of R, Z, and λ. As noted above, λ has been previously differenced radially on a mesh centered between R, Z nodes, which greatly improved the radial resolution. This could be done to second order accuracy (in $h_s = 1/[N_s-1]$) since no radial derivatives of λ appear in its defining equation, $J^s = 0$ (here, J^s is the contravariant radial component of the current). Near the

magnetic axis, however, a type of numerical interchange instability (mesh separation) has been observed as the angular resolution is refined. This behaviour has prevented the temporal convergence of 3D solutions with large numbers of poloidal (m) and toroidal (n) modes (typically, $m \sim 6\text{-}8$ was the practical limitation). It has also produced convergence problems for equilibria with low ι ($<<1$) where field lines must encircle the magnetic axis many times to define magnetic surfaces. The new differencing scheme computes the stream function on the same mesh as R and Z (although the output values of λ continue to be on the centered-grid for backwards compatibility), which leads to numerical stabilization of the origin interchange. To avoid first order errors (in h_s) near the plasma boundary resulting from the new representation of λ, the radial current J^s continues to be internally represented (in terms of λ) on the interlaced-grid. This maintains the good radial spatial resolution associated with the original half-grid representation for λ. As a result, computation of accurate, convergent solutions with substantially higher mode numbers is now possible using VMEC ($m < 20$). This corresponds to much finer spatial resolution and significantly improved force balance in the final equilibrium state. It also allows the calculation of equilibria with lower values of ι, which were difficult to obtain with the previous differencing scheme.

An additional improvement in the output from VMEC includes a recalculation (once the VMEC equilibrium has been obtained) of the magnetic force balance $\mathbf{F} \equiv \mathbf{J}\times\mathbf{B} - \nabla p = 0$. The radial ($\nabla s$) component of $\mathbf{F}$ is solved in terms of the non-vanishing contravariant components of B (B^u and B^v) and the metric elements determined by VMEC, as a magnetic differential equation for B_s. An angular collocation procedure (with grid points matched to the Nyquist spatial frequency of the modes) is used to avoid aliasing arising from nonlinear mode coupling of the Fourier harmonics of R and Z in the inverse representation of the equilibrium equation. The accurate determination of B_s, together with the higher angular resolution afforded by the larger limits on the allowable m,n spectra in VMEC, permits an accurate assessment for the parallel current (which contains angular derivatives of B_s) as a function of poloidal mode number, to be performed.

4.2 Bootstrap Current Profile

The current profiles for the NCSX design have been determined by a bootstrap current calculation using VMEC equilibria. Axisymmetric calculations using the bootstrap module in the jsolver code [3-5] have been used for this purpose. For perfect quasi-axisymmetry, the bootstrap current is identical to that in an equivalent tokamak, because the bootstrap current is determined by the Fourier components of mod(B) in Boozer coordinates. In practice, the quasi-axisymmetry condition is satisfied approximately. Fully three-dimensional Monte-Carlo-δf bootstrap calculations have been done for an earlier NCSX reference configuration, configuration C82, using the ORBIT code [6, 7] to quantify the errors introduced by the residual nonquasisymmetric ripple. These calculations have verified that the bootstrap current is given to a good approximation by the axisymmetric terms alone. The Monte-Carlo simulations for the non-axisymmetric case have been further benchmarked against calculations with the DKES (Drift Kinetic Equation Solver) code [8]. In calculating the bootstrap current with the jsolver code, the density profile has been taken to be $n(s) = n(0)(1\text{-}s^{2.3})^{0.1}$, where $n(0) = 0.54 \times 10^{20}$ m^{-3}.

The corresponding temperature profile for the full, 4% β, li383 case is $T(s) = T(0)(1-s^{2.3})^{1.9}$, where T(0) = 2.14 kev.

4.3 The PIES Code

Three-dimensional magnetic fields have magnetic islands and regions of stochastic field lines. The VMEC code uses a representation of the magnetic field that assumes nested flux surfaces. The PIES code is a three-dimensional equilibrium code that uses a general representation for the field, and is therefore capable of calculating islands and stochastic field line trajectories. There is an extensive set of publications on the algorithm, implementation, validation, convergence properties and applications of the PIES code. [9-13, 16-40]

The PIES code solves the MHD equilibrium equations using a Picard iteration scheme,

$$\nabla \times \mathbf{B}^{n+1} = \mathbf{J}(\mathbf{B}^{n}),$$

$$\nabla \cdot \mathbf{B}^{n+1} = 0,$$

where $\mathbf{B}^{n}$ is the magnetic field at the start of the n^{th} iteration, and $\mathbf{J}(\mathbf{B}^{n})$ is the current found from the force balance equation, $\mathbf{J} \times \mathbf{B} = \nabla p$, and the constraint $\nabla \cdot \mathbf{J} = 0$. This scheme is closely related to the Picard algorithm widely used to solve the axisymmetric Grad-Shafranov equation in the form $\Delta^* \psi_{n+1} = j_\phi(\psi_n)$. As with the Picard iteration scheme for the Grad-Shafranov equation, underrelaxation is used to extend the domain of convergence of the Picard iteration.

An advantage of the Picard scheme is that it provides an accurate calculation of resonant pressure driven currents, which are believed to play an important role in determining island widths At each iteration, the code solves for the current from the force balance equation. Writing $\mathbf{J} = \mu\mathbf{B} + \mathbf{J}_\perp$, $\mathbf{J}_\perp = \mathbf{B} \times \nabla p / B^2$ gives, $\mathbf{B} \cdot \nabla\mu = -\nabla \cdot \mathbf{J}_\perp$. Integration of this magnetic differential equation gives an accurate method for determining the currents. (Following the work of Gardner and Blackwell [41] demonstrating the importance of using an accurate solution for the currents in stability studies, it is now in fact routine in Mercier and global stability studies for stellarators to recalculate the current from three-dimensional equilibrium solutions in this way.) In implementing a numerical scheme for solving the magnetic differential equation, explicit upper bounds on the associated numerical errors were derived and are used to allow the specification of required tolerances in the code.[10]

As the PIES code iterates, the pressure and current are flattened in islands and stochastic regions. Several numerical diagnostics in the code allow the determination of the location of these regions. The PIES algorithm is described in detail in the references [9-13, 19].

The PIES code has been validated by testing of the individual components, by internal checks in the code that monitor the accuracy with which the equilibrium equations are satisfied, and by comparison with analytic solutions and with other codes. Analytic solutions against which the code has been compared have included Soloveev equilibria[11], large aspect ratio stellarator expansions[11], helical force-free Bessel function equilibria with islands[19], and the analytic solutions of White et al for saturated tearing modes with narrow islands. Comparison of

PIES with other codes has included: comparison with axisymmetric j-solver[14] equilibria for TFTR and DIII-D; comparison with Biot-Savart vacuum field solvers; comparison with marginal stability for tearing modes calculated by the linearized resistive time-dependent code of Hughes; and comparison with VMEC[16]. Ref. [16] contains a careful comparison between the VMEC code and the PIES code solutions. The devices modeled were the ATF and TJ-II stellarators, for transforms where low order rationals were absent. The flux surface shape, location of the magnetic axis and the value of iota as a function of flux surface were monitored as a function of β and radial resolution. An extrapolation in radial resolution was used to verify the quantitative agreement of the codes. The comparison with VMEC was continued in reference [18]. Here, the rotational transform as a function of radius was in excellent agreement between the two codes for the W7-X stellarator, at $< \beta > = 5\%$.

Many stellarators, for example ATF, TJ-II, W7-AS, W7-X and LHD have been modeled by the PIES code [11,16,18,20]. Present day experiments have not reached the predicted equilibrium beta limit, and no experimental study of this issue has therefore been possible.

In the context of the NCSX design effort, several modifications have been made to the PIES code that have increased its speed by about an order of magnitude, allowing routine application of the code to evaluate flux surfaces in candidate NCSX configurations. The speed of the code was improved by modifications to use an improved method for PIES initialization with a VMEC solution, to convert to a spline representation for field line following, and to store matrix inverses.

Compared with VMEC, the PIES code has a more time-consuming algorithm, which is needed for a general representation for the magnetic field. Time is saved by initializing PIES using a converged VMEC solution. For this purpose, the under-relaxation scheme in PIES has been modified to provided an improved coupling to the VMEC solution. This involves blending with the VMEC field in the first PIES iteration. The previous under-relaxation scheme blended the current rather than the fields. The under-relaxation was skipped in the first PIES iteration, allowing a large step from the VMEC field, and slowing the ultimate convergence. The PIES code follows magnetic field lines as a preliminary step to solving the magnetic differential equation determining the Pfirsch-Schlueter current. Conversion from a Fourier representation to a spline representation of the field has speeded ups the code by about a factor of two.

In each iteration of the PIES code, a discretized Ampere's law is solved by the inversion of a block-tridiagonal matrix. The elements of the blocks are determined by metric elements of a ``background coordinate system'' that does not change from one iteration to the next, allowing time to be saved by storing the inverses of the blocks. For high resolution calculations, this changes the scaling of the code's execution time from m^3n^3k to a much more favorable m^2n^2k where m and n are the number of the poloidal and toroidal modes retained, and k is the number of radial grid surfaces.

4.4 Flux Surface Integrity

Three-dimensional magnetic fields have magnetic islands and regions of stochastic field lines. It is desired to minimize the size of these regions in NCSX to obtain nested flux surface

across at least 90% of the cross-section. As a first step, a fixed boundary reference equilibrium with good flux surfaces was identified. Coils were reverse engineered to produce this configuration, and free-boundary evaluation with the PIES code was incorporated in the coil design process to ensure that flux surfaces were preserved. Trim coils have been added to the design to provide flexibility, preserving the flux surfaces for a range of configurations.

The configuration optimizer used to generate candidate configurations for the NCSX design study did not include a measure of flux surface integrity. Flux surface calculations for the various candidate configurations have found significant differences in the extent of islands and stochastic regions. This is illustrated by the calculations described in this section. The earlier reference configuration, C82, was found to have a large region of stochastic field lines at beta values of interest. This was typical of several types of configurations that were studied. In contrast, the flux surfaces of the NCSX reference design Configuration 383 and similar configurations were nearly adequate even before the application of any flux surface optimization. The residual islands could be removed by a small adjustment of the boundary shape which had little impact on the other physics propterties. Section 4.5 discusses the adjustment of the fixed boundary configuration and of the coils for healing the flux surfaces.

In regions where $d\iota/ds > 0$, perturbed bootstrap current effects are predicted to lead to substantially decreased magnetic island widths in configurations of the type studied here.[42] This is the inverse of the neoclassical tearing mode that has been observed in tokamak experiments. This neoclassical effect is being incorporated in the PIES code, but has not been included in any of the calculations reported here. The calculations are therefore conservative in that the calculated island widths are likely to be larger than would be observed in an experiment operated in a collisionless regime. Section 4.6 gives an estimate of the neoclassical effect on the island widths.

The PIES calculations discussed in this section are all fixed boundary, and used 143 Fourier modes, $0 \le m \le 11$, $-6 \le n \le 6$, and 60 radial zones.

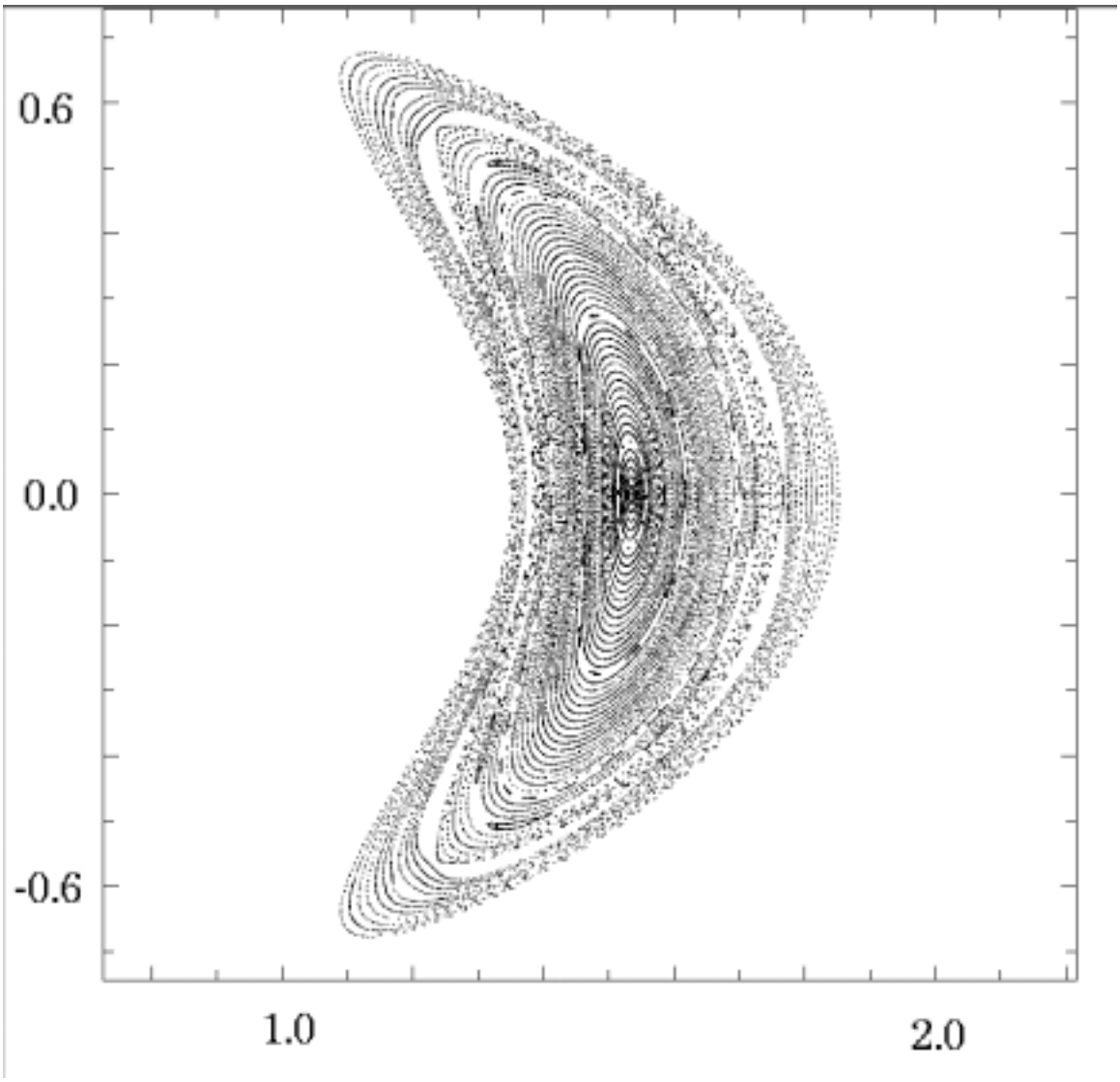

Figure 4-1. Poincare plot for configuration c82 at full current, $\beta = 0$

Figure 4-1 shows a Poincare plot of a fixed-boundary PIES equilibrium for Configuration C82 at full current, $\beta = 0$. Magnetic islands occupy about 10% of the cross-section. The islands are more readily visible if the Poincare plot uses a polar (ρ, θ) coordinate system, as in Figure 4-2. Here, the coordinate ρ is taken to be constant on VMEC flux surfaces, and to measure the distance of the VMEC flux surface from the magnetic axis along the $\theta = 0$, $\phi = 0$ line. The angular coordinate θ is identical to the VMEC angular coordinate. When plotted in these coordinates, the Poincare plot gives straight lines when the VMEC and PIES solutions coincide.

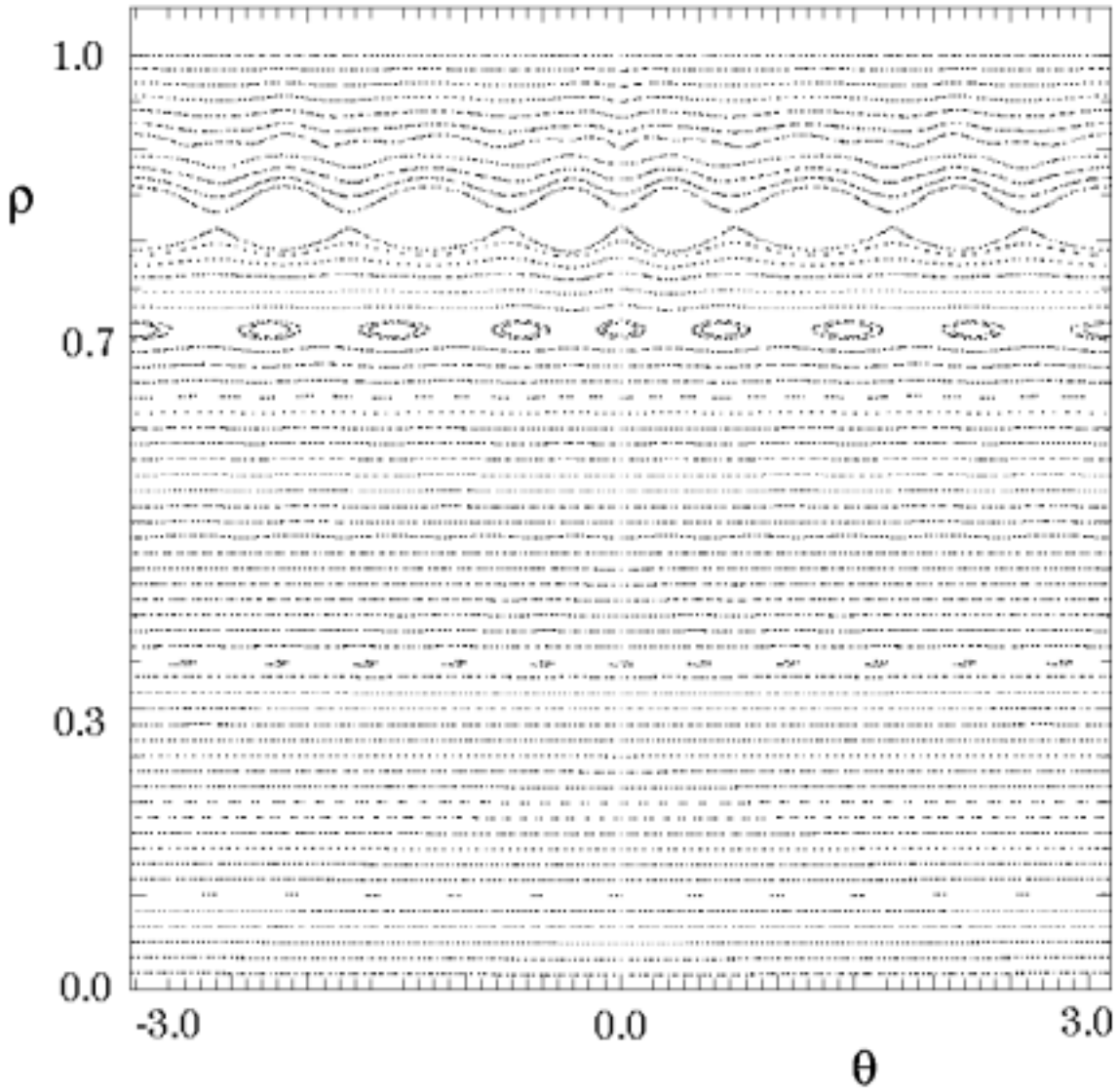

Figure. 4-2. Poincare plot for configuration c82 in VMEC coordinates, full current, β = 0

When β is raised to 3%, the PIES calculations find that a substantial fraction of the flux surfaces are lost (Figure 4-3). The equilibrium solution shown is not fully converged. The

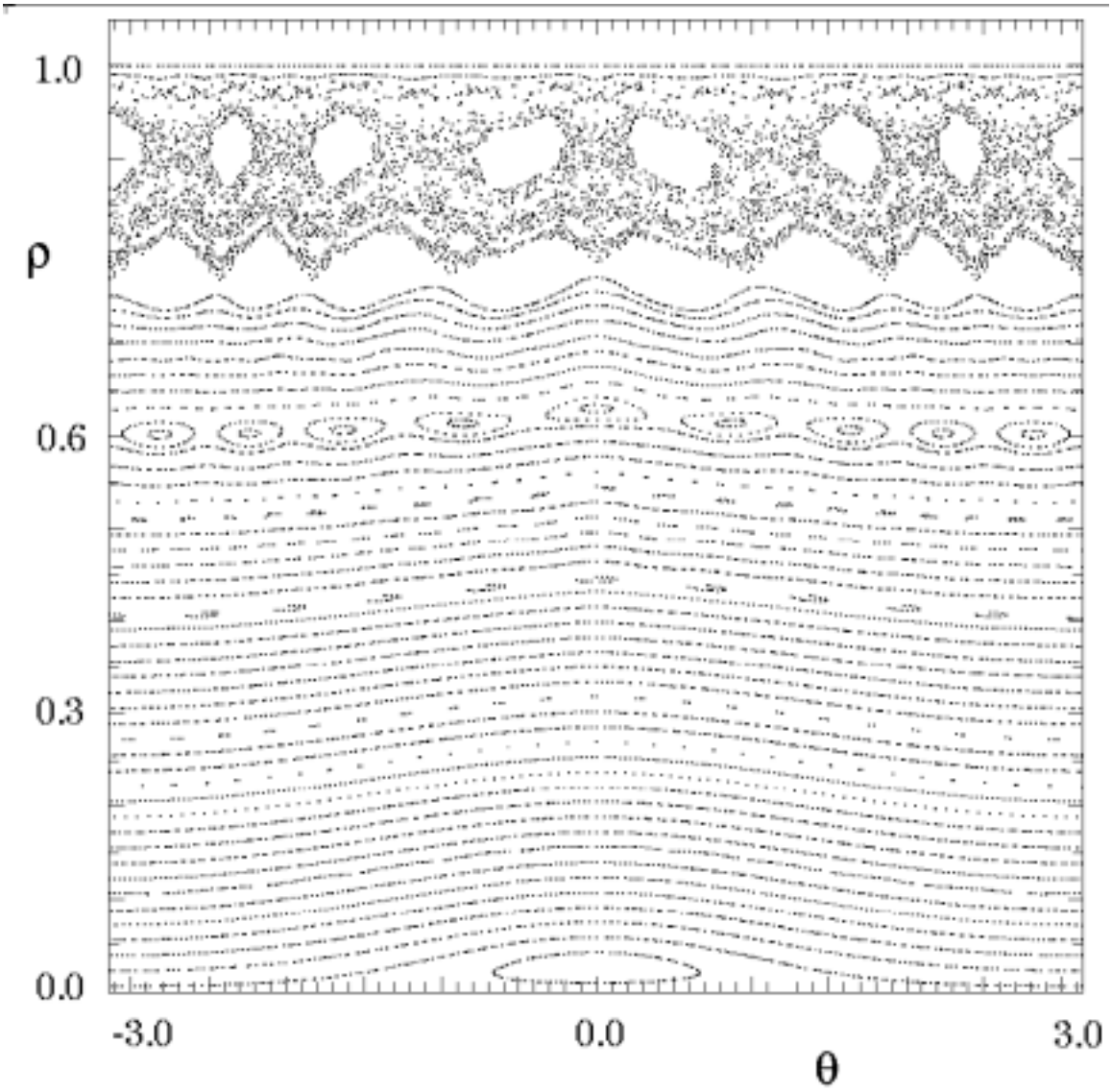

Figure 4-3. Poincare plot for earlier configuration, c82, at full current, β = 3%

outer surfaces continue to deteriorate as the calculation progresses, so that further computation is of limited interest. Flux surface integrity is a problem for configuration c82 in the absence of stabilizing neoclassical effects.

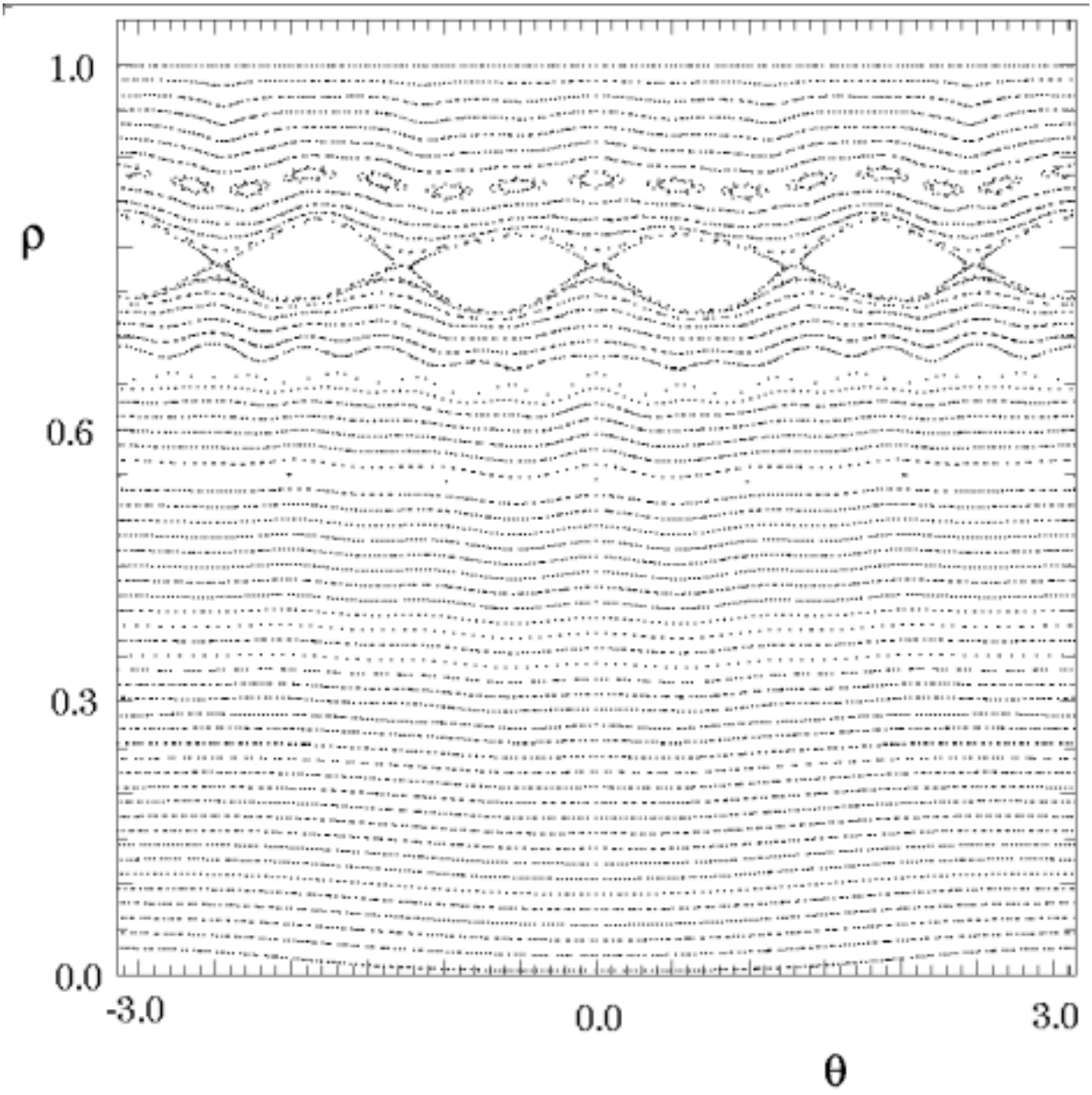

Figure 4-4. Poincare plot for configuration 383 at full current, β = 4.2%

Figure 4-4 shows the result of a PIES calculation for configuration 383 as originally generated by the optimizer at full current, β = 4.2%. The flux surfaces are greatly improved relative to those of configuration c82. The total island width is about 15%, and is dominated by a single island chain at ι = .6 having poloidal mode number m = 5 and toroidal mode number n = 3.

The fact that the flux surface loss in the original configuration 383 is dominated by a single island chain indicates that this can be further improved by adjusting the amplitude of the corresponding resonant Fourier mode in the specification of the boundary shape. This has been demonstrated, and is discussed in the next section.

4.5 Healing of Flux Surfaces

In this section we consider manipulation of the width and phase of magnetic islands in finite β stellarator equilibria by making small variations to the boundary or the coils. Computation of the MHD equilibrium is provided by the PIES code. Magnetic islands are controlled by controlling the resonant fields at the rational surfaces, and the resonant fields are calculated via construction of quadratic-flux-minimizing surfaces [43].

Magnetic islands are caused by resonant radial magnetic fields where the rotational transform is a rational value. The continuous one-dimensional family of periodic orbits that form a rational rotational transform flux surface in the absence of resonant fields will be reduced to a finite set of periodic orbits by the resonant field, and an island chain will form. The periodic orbits surviving perturbation will typically be the stable and unstable periodic orbits, which correspond to the O and X points on Poincare plots of the magnetic field. In the small island approximation, where the shear, ι', is assumed constant across the island, the width of the island is given [44] as $w \propto \sqrt{\{|B_{nm}|/ \iota\text{-}'m\}}$, where $B_{nm} = (\mathbf{B} \cdot \nabla s / \mathbf{B} \cdot \nabla \phi_{nm}$ is the resonant Fourier component of the radial field at the $\iota\text{-} = n/m$ rational surface, s is the radial coordinate, and the prime represents derivative with respect to s. The phase of the island chain is determined by the sign of B_{nm} and the sign of the shear. The manipulation of island width and phase is enabled via control of the magnitude and sign of the resonant field.

A method for calculating resonant fields at rational surfaces has been incorporated into PIES. This method is based on the construction of quadratic-flux-minimizing surfaces. The construction of these surfaces has been presented in Ref. 43, and for the purposes of this discussion it is sufficient to note that a rational quadratic-flux-minimizing surface passes directly through the corresponding island chain, and may be considered as a rational flux surface of an underlying unperturbed magnetic field. The resonant radial field is constructed as the field normal to the quadratic-flux-minimizing surface. In the following, the term 'resonant field' shall refer to the action gradient [2] as calculated during the construction of a given quadratic-flux-minimizing surface.

A set of islands that we wish to control is selected. Generally the lowest order resonances present will produce the largest magnetic islands. A convenient method of selecting the lowest order rationals is guided by the Farey Tree construction [45]. The corresponding set of resonant fields that need to be controlled is represented by $\mathbf{B} = (B_{n1m1}, B_{n2m2}, \ldots)^T$.

We expect that an (n,m) island width will be strongly affected by an (n,m) resonant deformation of the plasma boundary in magnetic coordinates and perhaps through coupling to neighboring modes, so a set of independent boundary variation parameters is constructed as follows. We consider the minor radius $r = \sum r_{nm} \cos(m\theta - nN\phi)$ of the plasma boundary to be a Fourier series in the cylindrical toroidal angle and the poloidal angle used in VMEC to construct

the input R and Z harmonics. The conversion to cylindrical space is given as $R = r\cos\theta$, $Z = r\sin\theta$. For a change $r \rightarrow r + \delta r_{nm}\cos(m\theta - n N \phi)$, the input Fourier harmonics for the VMEC code change according to $R_{m-1,n} \rightarrow R_{m-1,n}+\delta r_{nm}/2$, $R_{m+1,n} \rightarrow R_{m+1,n}+\delta r_{nm}/2$, $Z_{m-1,n} \rightarrow R_{m-1,n}-\delta r_{nm}/2$, $Z_{m+1,n} \rightarrow R_{m+1,n}+\delta r_{nm}/2$. In principle we may change infinitely many boundary harmonics r_{nm}, but a small set is chosen to match the islands that will be targeted and this becomes the vector of independent parameters $\mathbf{r} = (r_{n1m1}, r_{n2m2}, \ldots)^T$.

Now the problem is amenable to standard treatments where the functional dependence of **B** on **r** is represented

$$\mathbf{B}(\mathbf{r}_0+\delta\mathbf{r}) = \mathbf{B}(\mathbf{r}_0) + \mathbf{C}\cdot\delta\mathbf{r} + \ldots , \qquad (4\text{-}1)$$

where $\mathbf{r}_0 = 0$ is the initial boundary shape and $\delta\mathbf{r}$ is a small boundary variation. The coupling matrix **C** represents derivative information and will in general be an M ×N matrix, where M is the number of resonant fields, and N is the number of independent boundary variations. The jth column of the coupling matrix is determined through a VMEC/PIES run by making a small change δr_{njmj} and taking the difference in the resonant fields from the original equilibrium, divided by the change. Hence, N+1 VMEC/PIES runs are required to determine the coupling matrix.

The coupling matrix is inverted using the singular value representation [46], $\mathbf{C} = \mathbf{U}\mathbf{w}\mathbf{V}^T$, where U and V are ortho-normal and **w** is the diagonal matrix of singular values. If there are more variables than equations more than one solution may exist and the nullspace is spanned by the columns of U corresponding to zero singular values, of which there will be at least N-M.

Islands are removed if $\mathbf{B} = 0$, so by choosing a correction to the boundary $\delta\mathbf{r}$ according to

$$\delta\mathbf{r}_{i+1} = -\mathbf{V}\mathbf{w}^{-1}\mathbf{U}^T\mathbf{B}_i, \qquad (4\text{-}2)$$

where as in standard singular value decomposition techniques the zero, and if desired the small, eigenvalues are ignored in the inversion of **w**, and $\mathbf{B}_i$ is the vector of resonant fields at the ith iteration. In practice, several iterations will be required to achieve a desired accuracy.

This technique was applied to Configuration 383 A Poincare plot Figure 4-5 of the PIES field after 32 iterations shows island chains and the $\iota = 3/5$ island is quite large. In this and the other Poincare plots to be shown, the Poincare section is the $\phi = 0$ plane and 50 field lines are followed starting along the $\theta = 0$ line. In addition, field lines at the X points of several low order island chains are followed and the quadratic-flux minimizing surface and an estimated separatrix has been plotted over one period of each island chain. The separatrix of the island chains has been calculated using the resonant radial field and the shear at the rational surface of the VMEC equilibrium. PIES has not yet converged for this case, but the information about the island width is still useful for construction of the coupling matrix.

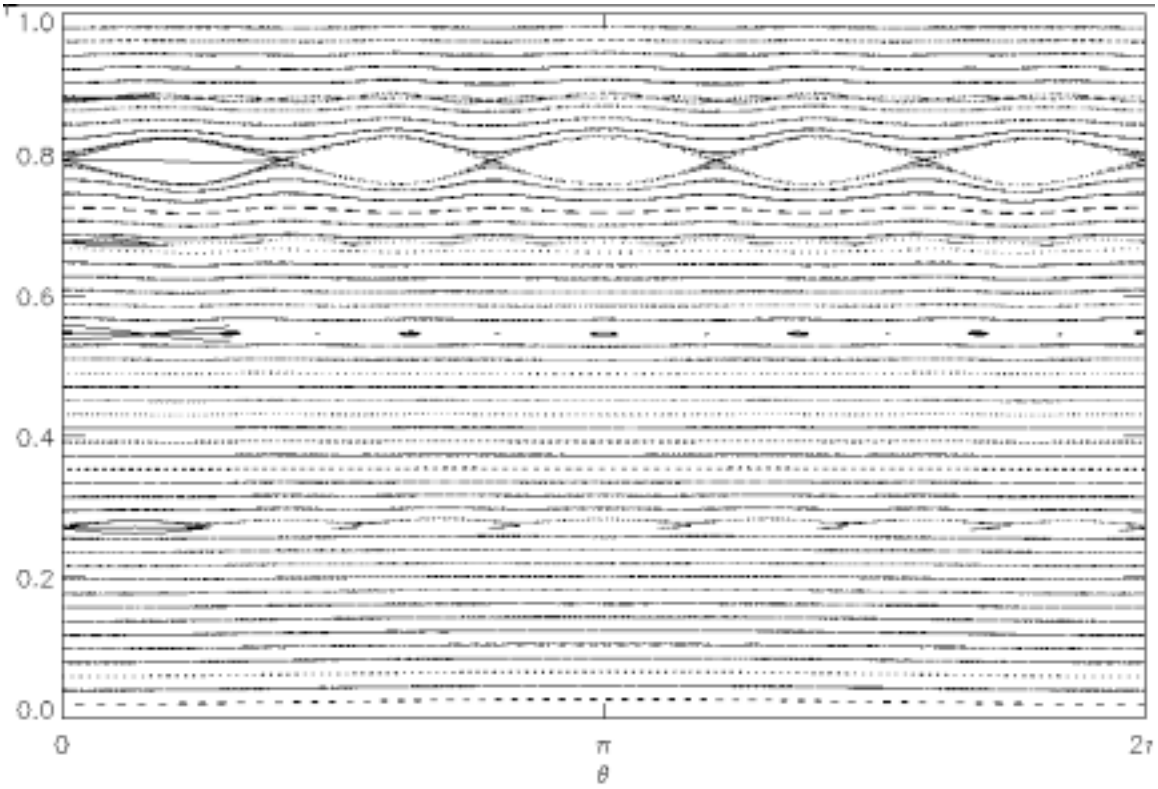

Figure 4-5. Poincare plot of initial li383 configuration after 32 PIES iterations

In this application of the island reducing technique, the (3,5),(6,10),(3,6) and (6,12) resonances are targeted, and the (3,9),(3,8),(3,7),(3,6),(3,5) and (3,4) boundary harmonics are varied. The (3,7) resonance is also present in the configuration, but this has not been targeted. The (6,10) resonance produces an island at the same rational surface as the (3,5), namely at $\iota = 3/5$, and may be considered as the second harmonic of the (3,5) resonance. If the (6,10) resonant field is not targeted, this may cause an island of distinct topology from the (3,5). For this set of resonant fields and independent boundary variation parameters, the coupling matrix is shown.

$$\begin{bmatrix} \delta B_{3,5} \\ \delta B_{6,10} \\ \delta B_{3,6} \\ \delta B_{6,12} \end{bmatrix} = \begin{bmatrix} -0.15603, & 0.94645, & -0.73397, & -1.13506, & -0.17282 & -0.30578 \\ 0.12627, & 0.17790, & 0.02146 & 0.19875, & -0.07025, & 0.01394 \\ -0.05487, & -0.22773, & -0.50056, & 0.24140, & -0.30079, & 0.01531 \\ -0.00874, & 0.03067, & -0.00351, & 0.00827, & -0.00327, & -0.00083 \end{bmatrix} \begin{bmatrix} \delta_{3,9} \\ \delta_{3,8} \\ \delta_{3,7} \\ \delta_{3,6} \\ \delta_{3,5} \\ \delta_{3,4} \end{bmatrix} \quad (4\text{–}3)$$

On performing the Newton iterations, the following reduction is observed.

iteration	$\lvert B_{3,5}\rvert$	$\lvert B_{6,10}\rvert$	$\lvert B_{3,6}\rvert$	$\lvert B_{6,12}\rvert$
0	1.8×10^{-3}	1.6×10^{-4}	1.3×10^{-4}	1.4×10^{-5}
1	1.3×10^{-4}	3.4×10^{-5}	1.0×10^{-4}	2.4×10^{-6}
2	6.7×10^{-5}	3.4×10^{-5}	5.1×10^{-5}	1.9×10^{-6}
3	2.4×10^{-5}	6.7×10^{-5}	4.0×1^{-16}	5.4×10^{-7}

(4-4)

The Newton iterations are terminated after four steps as this provides sufficient reduction of the islands as seen in Figure 4-6. In a true Newton iteration procedure, the coupling matrix would be re-calculated at every iteration. In this application such a procedure is too slow and the coupling matrix is not changed; nevertheless, the convergence is satisfactory. The total change in the boundary variation parameters is

$$\delta \mathbf{r} = (-0.00184,-0.00026,0.00056,0.00300,0.00012,0.00064)^{T}. \quad (4\text{-}5)$$

These variations are several millimeters in magnitude and generally have little impact on stability and other physics. However, the case shown does destabilize the ballooning modes on

some surfaces. This would be expected to relax the pressure gradient slightly on those surfaces. This is not surprising considering that the li383 configuration has been optimized to provide marginal ballooning stability at full pressure.

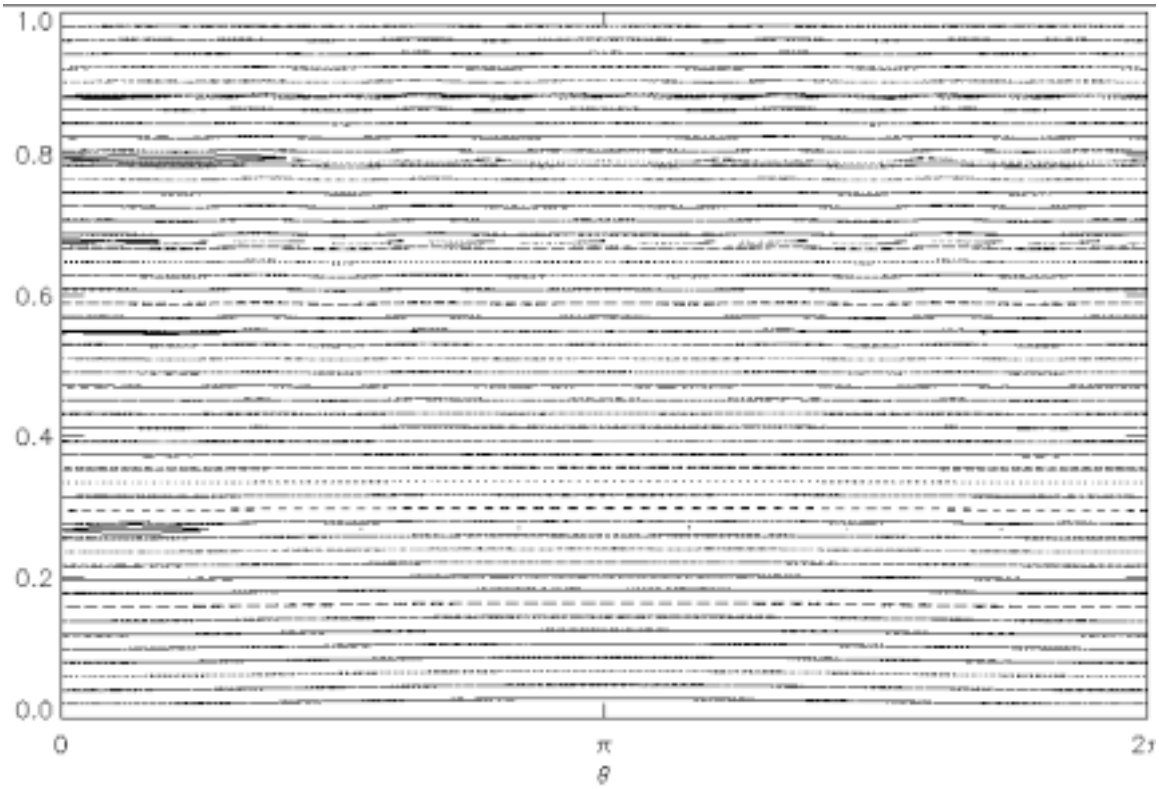

Figure 4-6. Poincare plot of full-beta island-reduced li383 configuration

The healed configuration has converged after 32 iterations. As mentioned, if the equilibrium has no islands, or if the width of the islands is less than the radial grid used in PIES, then PIES and VMEC will agree and PIES will rapidly converge. If the equilibrium displays islands and PIES is not fully converged, the island width after a given number of iterations is still sufficient for calculation of the coupling matrix and for the success of the Newton procedure in removing islands.

A similar procedure may be used to ensure coil designs are consistent with negligble island widths. A free-boundary implementation of PIES and a suitable parameterization of the coil geometry is used to optimize the coil design with respect to magnetic islands as follows.

A healed fixed boundary configuration is obtained as described above. It is important to note that such a boundary is consistent with there being no islands. Coils are designed to reconstruct a given boundary, but in general there will be some error - small but sufficient to excite islands at rational rotational transform surfaces. The free-boundary island healing approach will make small variations to the coil parameterization and examine the response of a chosen set of islands using free-boundary PIES calculations. The process is similar to the fixed boundary application, with the following differences.

The independent parameters that are varied alter the coil geometry, rather than the Fourier representation of the boundary, and optionally the coil currents. Also, in addition to eliminating resonant fields at rational rotational transform surfaces, it is convenient to require the plasma boundary created by the coils match the healed fixed boundary solution. To enable this, several Fourier modes representing the difference between the edge in free boundary calculation and the healed fixed boundary configuration are included in the target function to be zeroed.

The coils are represented by the following. The coils lie on a winding surface :

$$R = \sum_i \; r_i \cos(m_i \theta + n_i N \phi), \tag{4-8}$$

$$Z = \sum_i \; z_i \sin(m_i \theta + n_i N \phi), \tag{4-9}$$

and each coil has toroidal variation :

$$\phi_i = \phi_{i0} + \sum_k \; [\, \phi_{i,k,c} \cos(k \theta') + \phi_{i,k,s} \sin(k \theta')] \tag{4-10}$$

$$\theta' = \theta + \sum_j \; \theta'_j \sin(j \theta). \tag{4-11}$$

Typically a subset of the $\phi_{i,k,c}$ and $\phi_{i,k,s}$ modes is chosen to be the independent parameters.

The 0907 coils are considered. After 20 iterations the PIES field is shown in Figure 4-7. Varying only the $\{\phi_{i,k,c},\phi_{i,k,s}$; i = 1,2,3,4;k = 5,6,10$\}$ modes and targeting the (1,5), (1,6) resonances, the magnitudes of the resonant fields are reduced by several orders of magnitude, and the resulting 'healed' configuration is shown in Figure 4-8. To ensure that this results in a converged PIES equilibrium with small islands a fully converged PIES run is performed. Figure 4-9 shows the equilibrium after 400 iterations, after which it is well converged. As discussed in section 4.6, the small residual islands remaining in Figure 4-9 should be inconsequential.

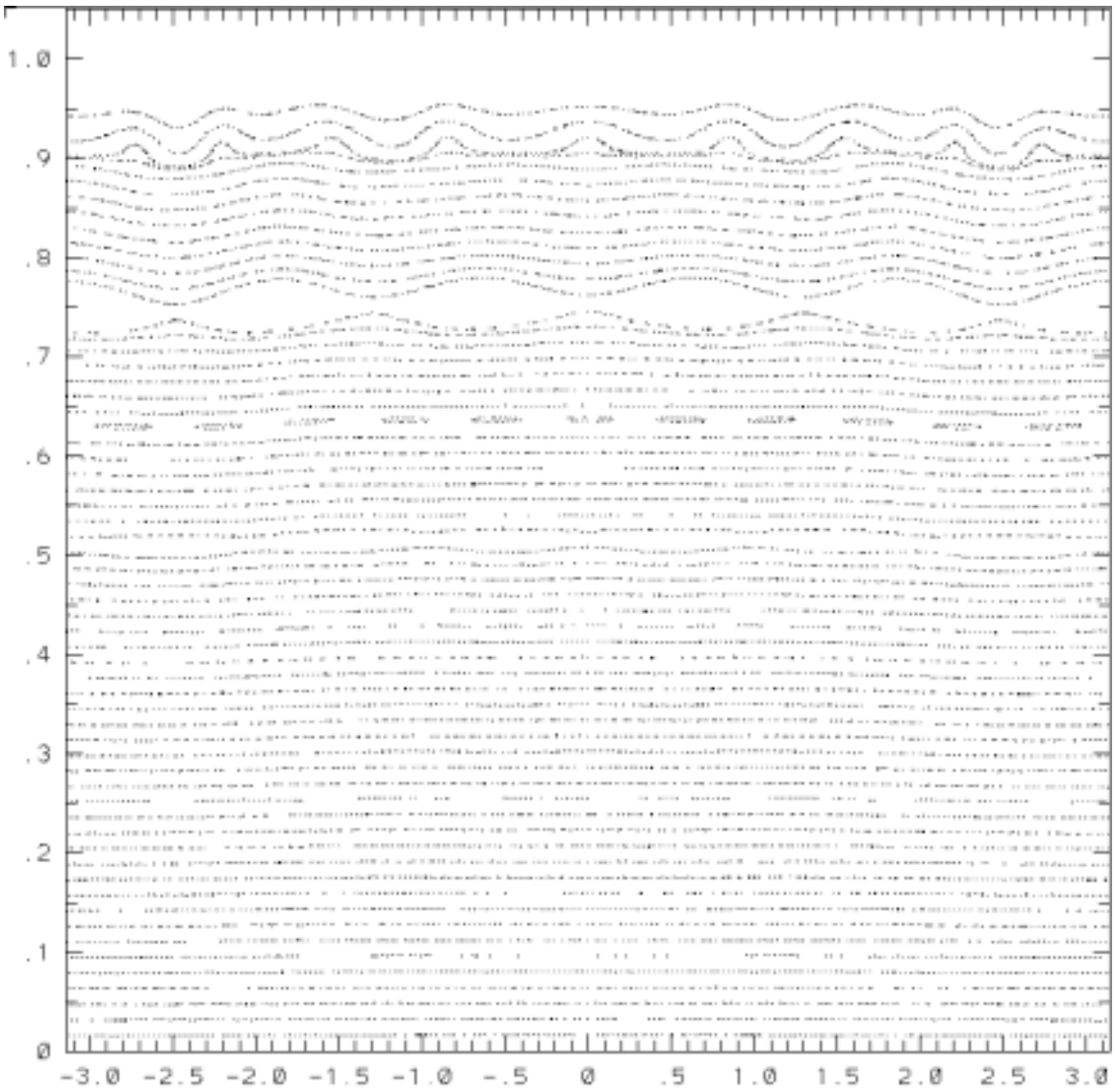

Figure 4-7. Poincare plot of free-boundary equilibrium with 0907 coil set after 20 iterations

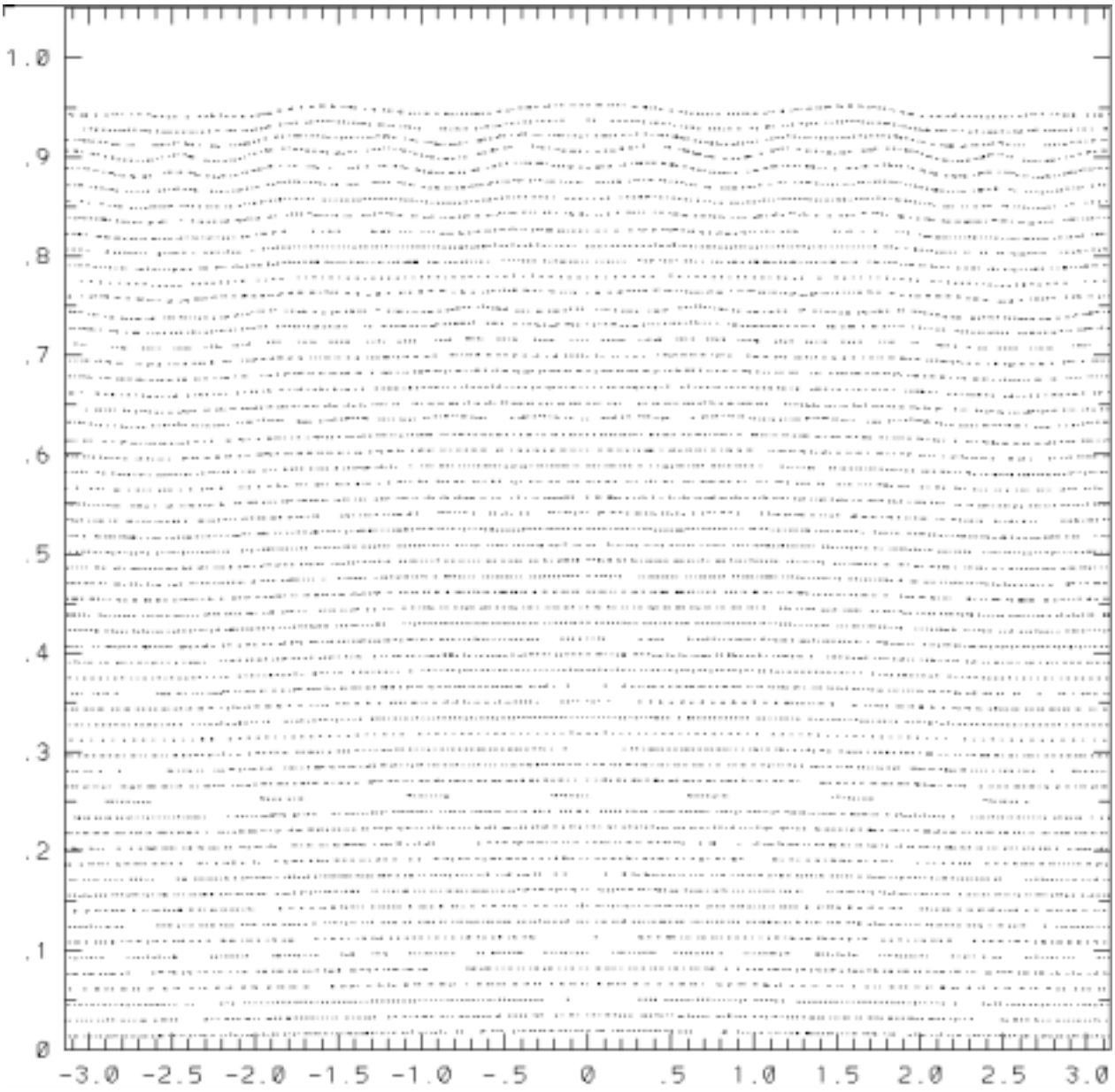

Figure 4-8. Poincare plot of free-boundary equilibrium with 0907 'healed' coil set after 20 iterations

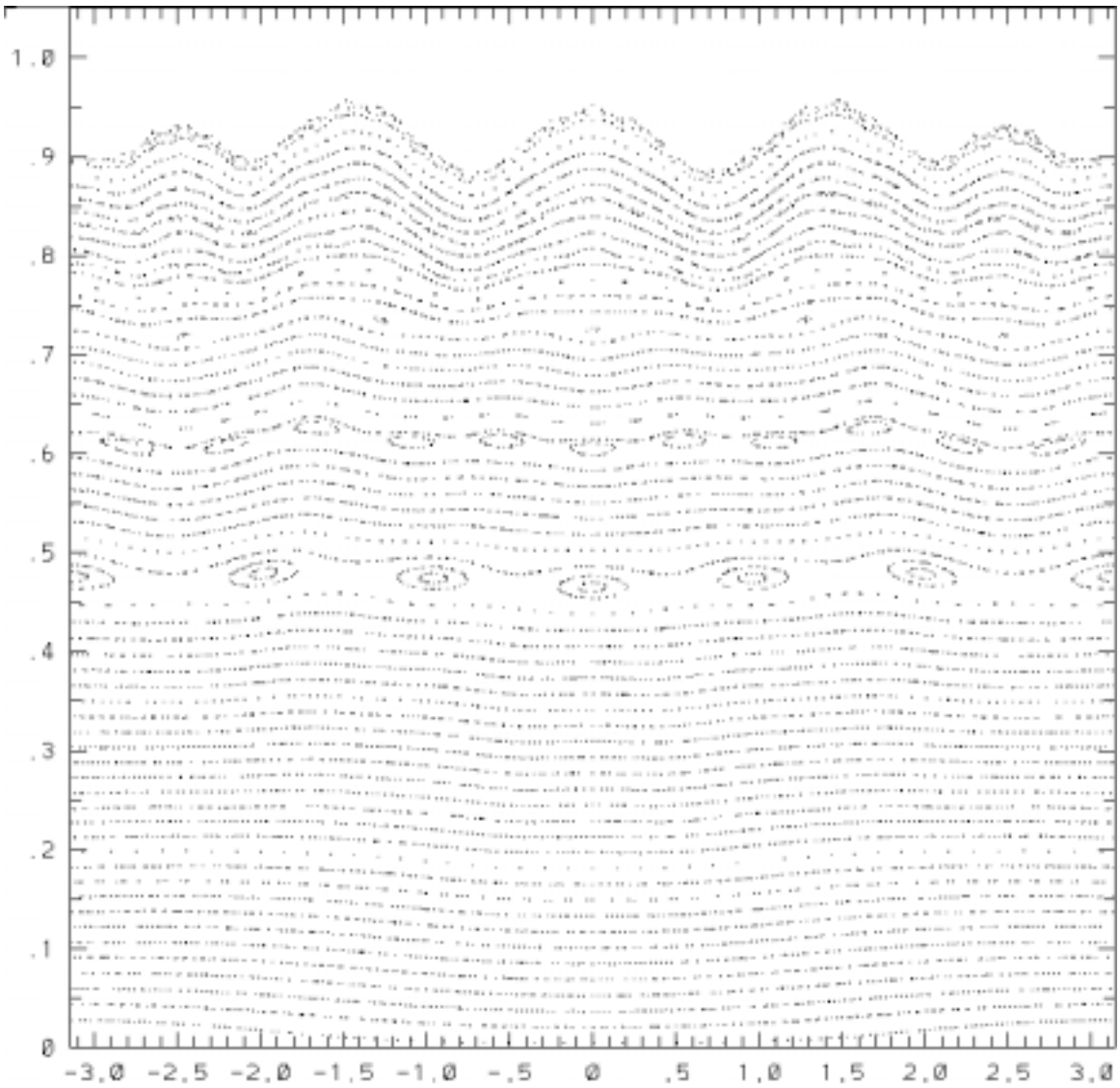

Figure 4-9. Poincare plot of converged free-boundary equilibrium with 0907 'healed' coil set

Figure 4-10 is a Poincare plot for the vacuum field produced by the 0907 "healed" coil set. The flux surfaces are regarded as quite adequate for startup.

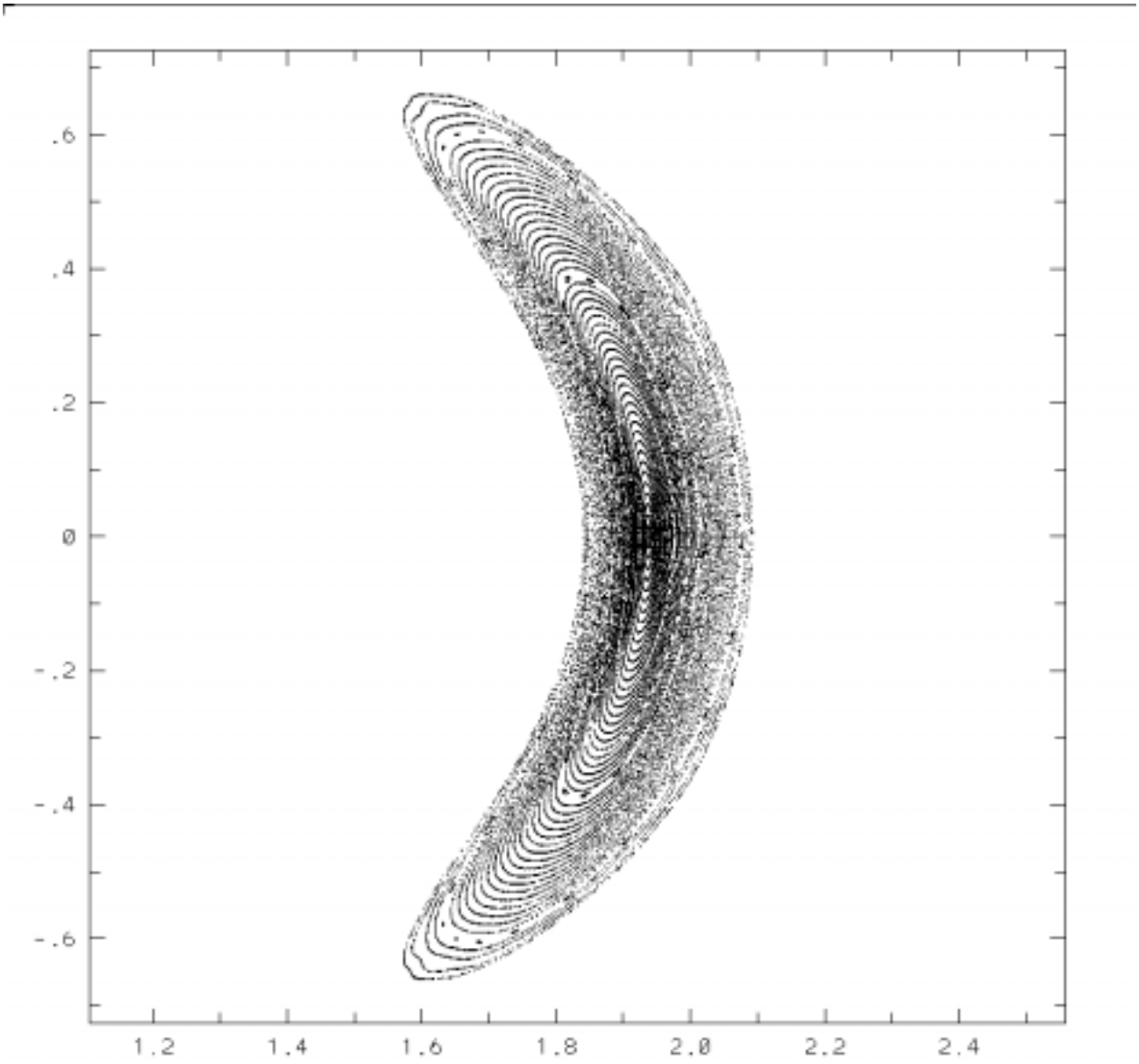

Figure 4-10. Poincare plot for the vacuum field produced by the "healed" 0907 coils

4.6 Neoclassical Healing of Magnetic Islands

4.6.1 Introduction

The purpose of this section is to estimate the effect of the neoclassical bootstrap current in reducing the width of magnetic islands produced by non-symmetric external field components in a quasi-axisymmetric stellarator such as NCSX. It has been recognized for some time [47] that the bootstrap current, which can destabilize "neoclassical tearing modes" in tokamaks, is stabilizing in a quasi-axisymmetric stellarator with outwardly increasing transform, i.e., positive

dι/dr. The magnitude of this effect depends on plasma collisionality, both through the dependence of the bootstrap current on the parameter ν_{*e} and through the role of finite parallel thermal conduction in limiting temperature flattening across the island.

In the present analysis, we employ the formalism of tokamak theory: the only stellarator-specific effect is an externally-imposed chain of magnetic islands with mode numbers corresponding to the dominant non-symmetric field "perturbation" in the NCSX configuration. For simplicity, we neglect two other effects, namely resonant Pfirsch-Schlueter currents and stabilizing resistive-interchange contributions, which are expected to be less important than the bootstrap current effect in the cases considered here.

4.6.2 Bootstrap Current Effect on Magnetic Islands

For cylindical tokamak geometry, including the bootstrap current density j_{bs}, the island width w in the weakly nonlinear regime [48,49,50] grows according to

$$(\mu_0 / 1.2\eta)\, dw/dt \;=\; \Delta' \;+\; 6.4\, (\mu_0 L_q / B_\theta)\, j_{bs} / w \qquad (4\text{-}12)$$

where Δ' is the usual tearing-mode stability quantity and $L_q = q/q'$. The numerical coeffficient 6.4 arises from calculating the applicable Fourier component of the current perturbation caused by zeroing the bootstrap current inside the magnetic island, i.e., within the area bounded by the island separatrix [51]. Writing

$$j_{bs} \;=\; -\; C_{bs}\, (\varepsilon^{0.5}/B_\theta)\, dp_e/dr \qquad (4\text{-}13)$$

where $\varepsilon = r/R$ and C_{bs} is a numerical coefficient of order unity which describes the dependences of the bootstrap current on the density and temperature profiles and on the collisionality parameter ν_{*e}, we obtain

$$(\mu_0 / 1.2\eta)\, dw/dt \;=\; \Delta' \;+\; 3.2\, C_{bs}\, \varepsilon^{0.5}\, \beta_{\theta e}\, (L_q / L_{pe}) / w \qquad (4\text{-}14)$$

where $L_{pe} = - p_e/p_e'$. For the tokamak ($q' > 0$), the bootstrap current term is positive and can overcome a negative Δ' to produce unstable neoclassical tearing modes. Comparisons with experimental data from tokamaks have generally suggested a numerical coefficient somewhat smaller than 3.2 in this equation; for example, analysis of neoclassical tearing modes in TFTR gave a coefficient of 2.6 [52]. For present purposes, however, we will retain the somewhat larger theoretical coefficient.

The case of an island produced by the vacuum magnetic fields in a quasi-axisymmetric stellarator may be considered analogous to the case of a tokamak in which an island is produced by superimposing an external helical magnetic perturbation that is resonant on a magnetic surface within the plasma. If such a perturbation were imposed dynamically, then the plasma would respond initially (i.e., within ideal-MHD theory) by forming a helical sheet current on the resonant surface. This sheet current would then decay resistively, producing a magnetic island; when the width of this island exceeds the very narrow resisitive layer of linear tearing-mode theory, it will be described by an appropriate generalization of the slow-growing tearing-mode

theory. In the present context, we are interested in the case where the resonant helical perturbation has mode numbers m and n for which the tearing mode would be stable, i.e., for which Δ' is negative. (Accordingly, we henceforth write $\Delta' = - |\Delta'|$.)

It is straightforward to extend the theory of weakly nonlinear tearing modes [47] to include an externally driven island. Rather than introducing the external perturbation explicitly, it is more convenient simply to describe it in terms of the island width w_{ext} that would be produced after resistive relaxation of the currents on the scale-length of the island but without the bootstrap current effects. Adding the bootstrap current term as before, the island is found to evolve according to

$$(\mu_0 / 1.2\eta)\, dw/dt \;=\; - \;|\Delta'|\,(1 - w_{ext}^2/w^2) \;-\; 3.2\, C_{bs}\, \varepsilon^{0.5}\, \beta_{\theta e}\, (L_\iota / L_{pe})\, /w. \qquad (4\text{-}15)$$

Here we have also written $L_q = - L_\iota = - \iota'/\iota$, in order to use the quantity $\iota = 1/q$ that is more appropriate to a stellarator and to indicate that in this case the bootstrap term is stabilizing. For a high-m mode, to a very good approximation, we may use

$$\Delta' \;=\; - \;2m / r\,. \qquad (4\text{-}16)$$

The "skin time" for resistive relaxation of w toward w_{ext} without bootstrap effects may now be estimated, namely $\tau_s = (\mu_0 / 1.2\eta)\, (2 w_{ext}\, r/m)$.

The bootstrap current term is seen to be inversely proportional to the island width w. This arises from the implicit assumption that density and temperature gradients are completely flattened across the magnetic island, thereby zeroing the bootstrap current within the island. Since electron thermal conduction is by far the fastest process of equilibration along field lines in high-temperature plasmas, bootstrap-current drive (or healing) of magnetic islands arises most effectively from the flattening of the electron temperature gradient, with flattening of the density gradient being less effective. Since in most practical cases (including the cases considered here) the electron temperature gradient provides the dominant contribution to the bootstrap current anyway, because the density profile is relatively flat, it is not unreasonable to employ the full bootstrap current in calculations such as these, but it should be recognized that this may give an over-estimate of the bootstrap-current effect on magnetic islands in some cases.

For very narrow islands, however, the path length along the helical field lines becomes very long, and finite (as distinct from effectively infinite) electron thermal conduction along the field lines will prevent the electron temperature from flattening fully across the island, thereby reducing even the most effective process of bootstrap-current island drive or healing. This effect is introduced into the theory [51] by modifying the bootstrap current term as follows:

$$1 / w \quad \Rightarrow \quad w / (w^2 + w_0^2) \qquad (4\text{-}17)$$

where we have defined a "critical island width" w_0, namely

$$w_0 \;=\; 5.1\, (\chi_\perp / \chi_{//})^{0.25}\, (\, R L_\iota / m \iota\,)^{0.5}. \qquad (4\text{-}18)$$

Here, $\chi_\perp$ and $\chi_{//}$ are the perpendicular and parallel thermal diffusivities, which control the degree to which the temperature is flattened across the island.

Setting dw/dt = 0, we then find the following relation to describe the actual island width w in terms of w_{ext} with bootstrap current effects included:

$$w_{ext}^2 / w^2 = 1 + 2 w_{bs}\, w / (w^2 + w_0^2), \tag{4-19}$$

where we have introduced an island width characterizing the bootstrap current effect, namely

$$w_{bs} = 1.6\, C_{bs}\, \varepsilon^{0.5}\, \beta_{\theta e}\, (L_\iota / L_{pe}) / |\Delta'|. \tag{4-20}$$

4.6.3 Assumed NCSX Parameters and Profiles

We have assumed the following parameters for the reference NCSX high-beta plasma:

$$\begin{aligned} &R = 1.4 \text{ m} \\ &a = 0.32 \text{ m (average)} \\ &\langle\beta\rangle = 4.2\ \% \\ &B_0 = 1.2 \text{ T} \\ &\langle n_e \rangle = 5.8 \times 10^{19} \text{ m}^{-3}. \end{aligned} \tag{4-21}$$

We have used density and temperature profiles that correspond very closely to those resulting from transport calculations for NCSX [53], namely:

$$\begin{aligned} n_e(r) &= 7.8\, (1 - r^2 / a^2)^{0.35} \qquad (10^{19}\ \text{m}^{-3}) \\ T_e(r) &= 2.8\, (1 - r^2 / a^2)^{1.35} \qquad (\text{keV}) \\ T_i(r) &= 1.9\, (1 - r^2 / a^2)^{0.75} \qquad (\text{keV}). \end{aligned} \tag{4-22}$$

The use of profiles that are parabolas raised to exponents α_n and α_T facilitates the calculation of the bootstrap current from the relevant theory. We have used an iota profile for the reference configuration for which the iota = 0.6 surface falls at r/a = 0.8 (see Section 3.1). The only other quantity needed from the iota profile is the local shear length, which for this profile is given by $L_\iota / a = 0.7$. It should be noted that the shear length L_ι may be longer for iota profiles that flatten or decrease toward the plasma edge.

4.6.4 Bootstrap Current Magnitude

To evaluate the bootstrap current term, i.e., the characteristic island width w_{bs}, it is essential to have a good estimate for the constant C_{bs}, since this can vary appreciably depending on profiles and on plasma collisionality. For present purposes, we have assumed the profiles given above and have employed the Hinton-Rosenbluth neoclassical theory for the "banana/plateau transition" [54], taking $Z_{eff} = 1.5$. We have allowed for T_i T_e and have

included both the ∇T_e and ∇T_i contributions to the bootstrap current. We obtain collisionality parameters (at the resonant surface r/a = 0.8) given by $\nu_{*e} = 0.49$ and $\nu_{*i} = 0.27$. For the profiles assumed and for these collisionality parameters, we than obtain $C_{bs} = 1.37$, which gives

$$w_{bs} / a = 0.28 . \qquad (4\text{-}23)$$

In practical units, the value of C_{bs} found here corresponds to a bootstrap current density at the resonant surface r/a = 0.8 given by $j_{bs} = 60$ A/cm^2. This value is close to the peak of the bootstrap current density profile in this case, because of the strong local pressure gradient and modest collisionality in the region of the resonant surface. This value agrees reasonably well with other calculations of the bootstrap current density in the NCSX reference configuration (see Section 4.3).

For the case considered here, the major contribution to the bootstrap current arises from the electron temperature gradient. This is partly because the density gradient is relatively small and partly because the coefficient in the transport matrix that multiplies the electron temperature gradient falls off less strongly with collisionality than does the coefficient multiplying the density gradient. The ion temperature gradient is found to make only a small contribution to the bootstrap current.

4.6.5 Critical Island Width w_0

To evaluate the critical island width, w_0, we need estimates for the perpendicular and parallel electron thermal diffusivities. We obtain an estimate for $\chi_\perp$ from its relation to the energy confinement time τ_E. Using $\tau_E \approx a^2 / 4\chi_\perp$ together with the empirically projected energy confinement time in NCSX of 25 msec, we obtain an estimate $\chi_\perp \approx 1.0$ m^2/s.

Obtaining a good estimate for $\chi_{//}$ is trickier. We start by calculating the Spitzer parallel electron thermal diffusivity at the resonant surface; this gives $\chi_{//}^{Sp} \approx 2.9 \times 10^9$ m^2/s. If we use this value in the expression for w_o, we would obtain $w_0 / a \approx 0.02$. However, at low collisionality, the electron mean-free-path typically exceeds the parallel wavelength along the helical perturbations. In such cases, the use of Spitzer thermal diffusivity may lead to unphysically large parallel heat fluxes, and thermal diffusion must effectively be replaced by thermal convection, according to the relationship $\chi_{//} \nabla_{//}^2 T_e \Rightarrow v_{the} \nabla_{//} T_e$, where v_{the} is the electron thermal velocity. The quantity $\nabla_{//}$ is the inverse parallel wavelength along the helical perturbation, which depends on the island width w and can be estimated as $\nabla_{//} \approx (mw/R)\, d\iota/dr = m\iota w/RL_\iota$. Since $\chi_{//}$ appears only to the one-quarter power, it is not necessary to retain this explicit dependence on the island width w and so, for present purposes, we simply estimate it as $w/a \approx 0.05$. For the "effective" thermal diffusivity in this convection-limited regime, we obtain $\chi_{//}^{eff} \approx 7.2 \times 10^7$ m^2/s. If we use this value in the expression for w_0, we would obtain $w_0 / a \approx 0.05$ (validating our estimate used to obtain $\chi_{//}^{eff}$).

Without more theoretical work, it is not obvious which value to use for w_0. Almost certainly, the Spitzer thermal diffusivity will overestimate parallel heat transport at low collisionality. On the other hand, fast electrons may still be able to equilibrate the temperature at a rate faster than that given by convection at the thermal speed. Accordingly, it might be

appropriate to take a range $w_0/a = 0.03 - 0.04$. In the calculation of the bootstrap island effect given below, we have simply chosen an intermediate value, namely:

$$w_0/a \approx 0.035. \tag{4-24}$$

It has been pointed out [55] that islands of width less than w_0 would not be expected to have a seriously deleterious effect on confinement because transport from one side of the island to the other along the direct path is already larger than transport along the path that follows the helical field lines. For the high-β NCSX reference case, this effect would apply only to islands with widths less than about 1 cm. However, the effect (unlike the bootstrap current) does not depend on the plasma beta-value and it increases strongly with higher collisionality, so it should apply particularly to low-temperature pre-heated plasmas. The Spitzer parallel thermal diffusivity scales as $T_e^{2.5}$, so a reduction in the temperature at the resonance surface to 100 eV (from 700 eV in the high-β plasma) would result in an increase in w_0/a to about 0.8. (Since parallel thermal convection scales much more weakly with electron temperature than thermal diffusivity, we find that the Spitzer diffusivity would be the operative process in this case.) This result suggests that in low-temperature ohmic plasmas in NCSX, islands at the iota = 0.6 surface as large as about 2.5 cm may not have a seriously detrimental effect on confinement.

4.6.6 Results for NCSX Reference Case

The actual island widths w for a range of possible "externally-produced" island widths w_{ext} are given in Table 4-1. For this calculation, we have taken $w_{bs}/a = 0.28$ and a value $w_0/a = 0.035$ (see the preceeding discussions). For external islands with widths in the range 2 - 6 cm (i.e., 6 - 18 % of the minor radius), the bootstrap current reduces the island width by almost a factor-of-three.

w_{ext} (cm)	w (cm)
1.0	0.41
2.0	0.70
3.0	1.00
4.0	1.34
5.0	1.73
6.0	2.19

Table 4-1. Neoclassical bootstrap-healed island widths w for various externally-generated island widths w_{ext} at the iota = 0.6 surface in the reference NCSX high-β configuration

4.6.7 Conclusions Concerning Neoclassical Healing

The depletion of bootstrap current within the island causes a substantial reduction in the width of the magnetic island caused by the dominant non-symmetric field "perturbation" in NCSX. Specifically, for the 4%-beta reference NCSX configuration, the bootstrap current should reduce the width of the m/n = 5/3 islands at the iota = 0.6 surface by almost a factor-of-three.

The bootstrap current in NCSX is sufficient for this purpose despite the relatively high collisionality of the plasma, which puts the island region (where $\nu_{*e} \approx 0.5$) in the "banana-plateau transition", rather than "pure banana", regime of neoclassical transport. For the cases considered, the main contribution to the bootstrap current comes from the electron temperature gradient, rather than the density gradient. The key element in ensuring sufficient bootstrap current is a relatively high value of the local $\beta_{\theta e}$ at the resonant surface together with a relatively steep local electron pressure gradient.

4.7 Conclusions

The VMEC code has been used for the routine calculation of three-dimensional equilibria for stability and transport studies. The PIES code has been used to calculate three-dimensional equilibria with islands and stochastic regions. Critical improvements have been made to both codes during the course of the NCSX design study. PIES calculations have found significant differences in the flux surface quality of candidate NCSX configurations, with the reference configuration, LI383, having particularly good flux surfaces. Judicious adjustment of the resonant field components has been used to heal the residual islands in this configuration. A set of trim coils provides the flexibility to generate a range of configurations with good flux surfaces. Neoclassical effects are estimated to provide additional suppression of magnetic islands.

References

[1] HIRSHMAN, S.P., Lee, D.K., Comput. Phys. Comm. **39** (1986) 143.
[2] HIRSHMAN, S.P., Van Rij, W.I. and MERKEL, P., Comp. Phys. Commun. **43** (1986) 143.
[3] KESSEL, C. E. Nuc. Fus., **34**, (1994) 1221.
[4] HIRSHMAN, S. Phys. Fluids, **31**, (1988) 3150.
[5] HARRIS, G. R. EUR-CEA-FC-1436, (1991).
[6] WHITE, R. B. AND CHANCE, M. S. Phys. Fluids **27**, (1984) 2455.
[7] WHITE, R. B. Phys. Fluids B **2**, (1990) 845.
[8] SPONG, D. http://www.pppl.gov/ncsx/Meetings/Physics_Mtgs/1999/June/june.html.
[9] REIMAN, A., and Greenside, H. S., Comput. Phys. Commun. **43** (1986) 157.
[10] REIMAN, A., and Greenside, H. S., J. Comput. Phys. **75** (1988) 423.
[11] GREENSIDE, H., REIMAN, A., and SALAS, A., J. Comput. Phys. **81** (1989) 102.
[12] Reiman, A. and Pomphrey, N. J. Comput. Phys. **941** (1991) 225.
[13] MONTICELLO, D. A., MERKEL, P., JOHNSON, J. L., and REIMAN, A. H., Proceedings of Tenth International Conference on Stellarators, Madrid (1995).
[14] DELUCIA, J., JARDIN, S. C., and TODD, A. M. M., J. Comput. Phys. **37** (1980) 183.
[15] CHODURA, R. and SCHLUTER, A., J. Comput. Phys. **41** (1981) 68.
[16] JOHNSON, J. L., MONTICELLO, D. A., REIMAN, A. H., et al., Comp. Phys. Commun. **77** (1993) 1.
[18] MERKEL, P., JOHNSON, J. L., MONTICELLO, D. A., et al., Proceedings of the Fourteenth International Conference on Plasma Physics and Controlled Nuclear Fusion Research paper IAEA-CN-60 | D-P-II-10 (1994).

[19] REIMAN, A. H. and GREENSIDE, H. S., J. Comput. Phys. **87** (1990) 349.
[20] JOHNSON, J. L., MONTICELLO, D. A., and REIMAN, A. H., Proceedings of the 15th International Conference on the Numerical Simulations of Plasmas (1994).
[21] A. H. Reiman and H. S. Greenside, J. Comput. Phys. **87** (1990) 349.
[22] A. H. Reiman and D. Monticello, Phys Fluids B **3** (August 1991) 2230.
[23] A. H. Reiman and D. Monticello, Nucl. Fusion **32** (1992) 1341.
[24] R. J. Goldston, et al Fusion Technol. **21** (May 1992) 1039.
[25] A. Lopez Fraguas, A. Salas, A. H. Reiman, D. A. Monticello, and J. L. Johnson, in Proceedings of the Ninth Kiev International Conference on Plasma Theory, July, 1992, p. I-577.
[26] S. C. Jardin, et al in Proceedings of the Fourteenth International Conference on Plasma Physics and Controlled Nuclear Fusion Research, (Wurzburg, Germany, September 1992) (International Atomic Energy Agency, Vienna, Austria), Paper IAEA-CN-56/D-4-13.
[27] D. A. Monticello, A. H. Reiman, and C. Y. Wang, in Proceedings of the Ninth International Workshop on Stellarators, (International Atomic Energy Agency, Vienna, Austria, 1993), p. 114.
[28] A. Salas, A. Lopez Fraguas, A. H. Reiman, D. A. Monticello, and J. L. Johnson, in Proceedings of the Ninth International Workshop on Stellarators, (International Atomic Energy Agency, Vienna, Austria, 1993) p.127.
[29] P. Merkel, J. L. Johnson, D. A. Monticello, and A. H. Reiman, in Proceedings of the Ninth International Workshop on Stellarators, (International Atomic Energy Agency, Vienna, Austria, 1993), p. 133.
[30] J. L. Johnson, D. A. Monticello, A. H. Reiman, and C. Wang, in Proceedings of the Ninth International Workshop on Stellarators, (International Atomic Energy Agency, Vienna, Austria, 1993), p. 121.
[31] J. L. Johnson, D. A. Monticello, A. H. Reiman, A. Salas, A. L. Fraguas and S. P. Hirshman, Comp. Phys. Commun. **77** (September 1993) 1.
[32] J. A. Schmidt, et al, J. Fus. Energy **12** (1993) 221.
[33] J Nuhrenberg, et al, Plasma Physics and Controlled Fusion, **35** Supplement (December 1993) B115.
[34] J. Manickam, et al, Phys. Plasmas **1** (1994) 1601.
[35] P. Merkel, J. L. Johnson, D. A. Monticello, A. H. Reiman, A. Salas, and A. L. Fraguas, Proceedings of the Fifteenth International Conference on Plasma Physics and Controlled Nuclear Fusion Research, (International Atomic Energy Agency, Vienna, Austria, September 1994).
[36] D. A. Monticello, J. L. Johnson, A.H.Reiman, and P.Merkel, in Proceedings of the Tenth International Workshop on Stellarators, EUR-CIEMAT **30** (1995) p. 45.
[37] R. J. LaHaye et al, in Proceedings of the Sixteenth IAEA Fusion Energy Conference, (International Atomic Energy Agency, Vienna, Austria, 1996) Paper F1-CN-64/AP1-21.
[38] A. Reiman, L.P. Ku, D. Monticello, C. Nuehrenberg, and W. Cooper, Plasma Physics Reports **23** (1997) 472.
[39] S. Arndt, P. Merkel, D. A. Monticello and A. H. Reiman, Phys. Plasmas **6** (1999) 1246.
[40] A. Reiman, et al, Phys. Plasmas **8** (2001).
[41] H. Gardner and B. Blackwell, Nucl. Fusion **33** (1993).
[42] C. C. Hegna and J. D. Callen, Phys. Plasmas **1** (1994) 3135.

[43] S.R. Hudson and R.L. Dewar. Analysis of perturbed magnetic fields via construction of nearby integrable field. *Phys.Plasmas*, **6(5)** (1999) 1532.
[44] A.J. Lichtenberg and M.A. Lieberman. *Regular and Chaotic Dynamics, 2nd ed.* Springer-Verlag, New York, 1992.
[45] J.D. Meiss. Symplectic maps, variational principles & transport. *Reviews of Modern Physics*, **64(3)** (1992) 362.
[46] W. H. Press, B. P. Flannery, S. A. Teukolsky, and W. T. Vetterling. *Numerical Recipes in Fortran 77 : The art of scientific computing*. Cambridge University Press, Cambridge, U.K.
[47] C. C. Hegna and J. D. Callen, Phys. Plasmas **1** (1994) 3135.
[48] P. H. Rutherford, Phys. Fluids **16** (1973) 1903.
[49] J. D. Callen, et al., in "Plasma Physics and Controlled Nuclear Fusion Research", Kyoto (IAEA, Vienna, 1987). **2**, p. 157.
[50] C. C. Hegna, et al., Plasma Phys. Controlled Fusion **35** (1993) 987.
[51] R. Fitzpatrick, Phys. Plasmas **2** (1995) 825.
[52] Z. Chang, et al., Phys. Rev. Lett. **74** (1995) 4663.
[53] D. R. Mikkelson, NCSX Project Meeting (January, 2001); see also Section 8.
[54] F. L. Hinton and M. N. Rosenbluth, Phys. Fluids **16** (1973) 836.
[55] R. J. Goldston, private communication (June, 2000).